Enhanced Photocatalytic Degradation Activity of BiFeO$_3$ Microspheres by Decoration with g-C$_3$N$_4$ Nanoparticles

Lijing Di[a,b], Hua Yang[a]*, Tao Xian[b] , Xiujuan Chen[a]

[a]*State Key Laboratory of Advanced Processing and Recycling of Non-ferrous Metals, Lanzhou University of Technology, Lanzhou 730050, China*
[b]*College of Physics and Electronic Information Engineering, Qinghai Normal University, Xining 810008, China*

In this work, the g-C$_3$N$_4$ nanoparticles decorated BiFeO$_3$ microspheres composites (g-C$_3$N$_4$/BiFeO$_3$) were successfully synthesized by hydrothermal treatment of g-C$_3$N$_4$ nanoparticles together with BiFeO$_3$ microspheres. The SEM and HRTEM observation indicate that the C$_3$N$_4$ nanoparticles with size of 30-50 nm are well decorated on the surface of BiFeO$_3$ microspheres. The photocatalytic activities of the samples are investigated by the degradation of methylene blue (MB) under the irradiation of simulated sunlight. The as-prepared g-C$_3$N$_4$/BiFeO$_3$ composites exhibit remarkable enhanced photocatalytic activity compared with bare BiFeO$_3$. More importantly, the photocataltic performance of the composites is further confirmed by the degradation of colorless phenol. Furthermore, the favorable catalytic stability of composites is demonstrated through the recycling photocatalytic experiment. The enhanced photocatalytic activity of g-C$_3$N$_4$/BiFeO$_3$ composites is mainly attributed to the separation of the photogenerated electron-hole pairs, resulting from the migration of the photoinduced charge between g-C$_3$N$_4$ nanoparticles and BiFeO$_3$. A possible photocatalytic mechanism for dye degradation over g-C$_3$N$_4$/BiFeO$_3$ composite is proposed based on the active species trapping experiment, revealing that the photogenerated hole (h$^+$) and hydrogen peroxide (H$_2$O$_2$) are regarded as the major active species for the decomposition of dye, while hydroxyl radicals (•OH) plays a minor role in the photocatalytic reaction.

Keywords: *BiFeO$_3$, g-C$_3$N$_4$ nanoparticles, composite, photocatalysis.*

1. Introduction

Semiconductor based photocatalysis has attracted considerable attentions owing to its promising application in solar energy conversion and environmental purification[1-6]. Perovskite oxide has been proven to be an important class of photocatalysts[7]. As one of the perovskite photocatalysts, BiFeO$_3$ exhibits visible-light-driven photocatalytic activity for the degradation of dyes and water splitting due to its narrow bandgap and chemical stability[8-11]. In addition to its photocatalytic property, BiFeO$_3$ has been also known to be a famous room-temperature multiferroic material[12]. However, the photocatalytic performance of bare BiFeO$_3$ is not satisfactory owing to high recombination rate of photogenerated electron-hole pairs, and this shortage limits its practical applications in the field of photocatalysis. Therefore, many strategies have been employed to suppress the recombination of photoinduced charges[13-19]. Among these methods, coupling BiFeO$_3$ with narrow-bandgap semiconductor of suitable band potential including BiVO$_4$, Ag/AgCl, Fe$_2$O$_3$ and Bi$_2$Fe$_4$O$_9$ is demonstrated to be an efficient way to promote photogenerated charges migration and separation, and then improve its photocatalytic activity[16-19].

Recently, A metal-free organic semiconductor photocatalysts, graphite-like carbon nitride (g-C$_3$N$_4$) with small bandgap of 2.7 eV, has been found to be a promising candidate for photocatalytic applications because of its narrow bandgap, non-toxicity, low cost and excellent chemical stability[20,21]. Particularly, it can be easily obtained by the heat treatment of nitrogen-rich precursors at relatively low temperature[20,21]. More importantly, g-C$_3$N$_4$ has been frequently employed as an ideal narrow-bandgap cocatalyst to combine with appropriate photocatalysts to form heterostructured composites with enhanced photocatalytic performance[22,23]. It is worth noting that energy-band potentials of g-C$_3$N$_4$ and BiFeO$_3$ are well-matched[24,25]. This suggests that the composites constructed by the two photocatalysts are expected to exhibit favorable photocatalytic performance. Wang et al. firstly reported that the bulk g-C$_3$N$_4$/BiFeO$_3$ composite can achieve the efficient separation of photoinduced charges[24]. It is generally accepted that the photocatalytic performance of g-C$_3$N$_4$/metal oxides composites strongly related to the morphology and size of g-C$_3$N$_4$[23]. Especially for the nanoscale g-C$_3$N$_4$ (such as nanosheets and nanoparticles), these materials possess large specific surface area, and thus provide more available surface active sites for the photocatalytic reaction and larger contact area for photogenerated charges transformation[23,26]. Until now, g-C$_3$N$_4$ nanosheets have been successfully combined

*e-mail: hyang@lut.cn

with $BiFeO_3$ to form $g-C_3N_4$ nanosheets/$BiFeO_3$ composites, and the composites exhibit enhanced photocatalytic activity towards the dye degradation[25]. To the best of our knowledge, however, the enhanced photocatalytic activity of $BiFeO_3$ by decorated with $g-C_3N_4$ nanoparticles is rarely reported.

In this work, the $g-C_3N_4$ nanoparticles decorated $BiFeO_3$ microspheres ($g-C_3N_4$/$BiFeO_3$) composites with enhanced photocatalytic activity were prepared. The methylene blue (MB) and colorless phenol were selected as model pollutant to evaluate the photocatalyic properties of the composites under simulated sunlight irradiation. The promotion mechanism of $g-C_3N_4$ nanoparticles on the photocatalytic performance of $BiFeO_3$ microspheres was investigated in detail.

2. Experimental Section

2.1 Chemicals

All raw materials were purchased from Sinopharm Chemical Reagent Co., Ltd, which were analytical reagents and used without any purification.

2.2 Synthesis of $g-C_3N_4$ nanoparticles

The bulk $g-C_3N_4$ was prepared by directly heating melamine in a semiclosed system[27]. Briefly, about 5 g of melamine was put into a corundum boat with a cover and calcinated at 520 °C for 4 h. After the reaction, the product was ground and collected for further use.

The $g-C_3N_4$ nanoparticles were synthesized via the treatment of bulk $g-C_3N_4$ in H_2SO_4. 1 g of bulk $g-C_3N_4$ was added into 50 mL of H_2SO_4 (98 wt %) and magnetically stirred for 10 h. Subsequently, the mixture was ultrasonicated for 10 h. During the ultrasonic process, the color of the suspension was changed from yellow to slight yellow. After that, the as-prepared suspension was placed for 12 h to obtain the flocculent precipitate, and the absorbance was removed. The obtained precipitate was washed several times with distilled water to near-neutral pH, and then dried at 60°C for 12 h to obtain final $g-C_3N_4$ nanoparticles.

2.3 Synthesis of $g-C_3N_4$ nanoparticles/$BiFeO_3$ composites

The $BiFeO_3$ microspheres were fabricated according to the hydrothermal route described in the literature[28]. Then the $g-C_3N_4$/$BiFeO_3$ composites were prepared as follows: a certain amount of $g-C_3N_4$ nanoparticles were added into 40 ml of distilled water and then ultrasound for 2 h. Subsequently, $BiFeO_3$ microspheres were dispersed into the above suspension under magnetically stirring. After the suspension was uniform, this mixture was transferred into a 50 ml Te flon-lined stainless steel autoclave and heated at 130°C for 2 h. Finally, the obtained precipitate were collected by centrifugation and dried at 70°C for 10 h to get the composites. To study the effect of the $g-C_3N_4$ nanoparticles

content on the photocatalytic activity of the composites, a series of sample were prepared with different $g-C_3N_4$ mass ratios of 4 %, 8 %, 16 % and 24 % ($m_{g-C3N4}/(m_{g-C3N4}+m_{BiFeO3})$) and the corresponding samples were named as 4CN/BFO, 8CN/BFO, 16CN/BFO and 24CN/BFO, respectively.

For comparison, sample 16CN/BFO was synthesized under the same condition mentioned above except that the $g-C_3N_4$ nanoparticles were replaced by bulk $g-C_3N_4$, and this sample is termed as 16bulkCN/BFO. On the other hand, the sample denoted M16CN/BFO was fabricated by direct mixing of $BiFeO_3$ microspheres and $g-C_3N_4$ nanoparticles ($m_{g-C3N4}/(m_{g-C3N4}+m_{BiFeO3})$ =16 %).

2.4 Characterization

The phase purity of the samples was detected by X-ray diffractometer (Bruker D8 Advance XRD). The field mission scanning electron microscope (JEOL JSM-6701F FE-SEM) and transmission electron microscope (JEOL JEM-2010 TEM) was employed to observe the morphology and structure of the products. Fourier transform infrared spectroscopy (FTIR) analysis was performed on a Bruker IFS 66v/S spectrometer. A UV-visible spectrophotometer with an integrating sphere attachment (PERSEE TU 1901) was used to measure the diffuse reflectance spectra of the samples.

2.5 Photocatalytic activity test

The photocatalytic activities of samples were evaluated by the degradation of MB and phenol under the simulated sunlight irradiation of a 300 W xenon l amp. In a typical experiment, the sample (0.1 g) was added into the solution of MB or phenol (200 mL, 5 mg/L). Before the photocatalytic reaction, the mixture was magnetically stirred in dark for 0.5 h to reach the adsorption-desorption equilibrium of organic molecule on the surface of catalysts. Under the simulated sunlight irradiation, a small amount of reaction solution was taken at a given time intervals and centrifuged at 6000 rpm/min for 10 min to separate the photocatalysts. During the photocatalytic reaction, the xenon lamp was cooled with water-cooling system to keep the solution at room temperature (~ 20°C). The concentrations of MB and phenol were measured by detecting the absorbance of the supernatant at a given wavelength ((λ_{AO7} = 665 nm and λ_{phenol} = 270 nm) on an UV-visible spectrophotometer. In order to evaluate the photocatalytic reusability of the samples, the recycling catalytic experiments toward the degradation of MB were carried out under the same conditions. After the first catalytic experiment, the photocatalyst in the reaction solution was recovered by centrifugation (6000 rpm/min, 10 min), washing with distilled water and drying in an oven (70°C, 10 h). The collected photocatalyst was dispersed into the fresh MB solution for the next cycle of the catalytic experiment. In the 1st run, the photocatalysts was 100% used. The recovery percentage of photocatalysts for 2nd, 3rd, 4th and 5th run was ~ 97 %, ~ 93 %, ~ 87 % and ~ 82 %, respectively.

To detect the active species formed in this photocatalytic reaction, ammonium oxalate (AO, 2mM) and ethanol (10 % by volume) were introduced aiming to trap photogenerated hole (h^+) and hydroxyl radicals (•OH), respectively[29,30]. Furthermore, the N_2 purging experiment (0.1 L/min) was also performed to expel the effect superoxide radicals (•O_2^-) and/or hydrogen peroxide (H_2O_2) on the photocatalytic degradation. The active species trapping experiments procedure were similar to the above photocatalytic experiment process.

3. Results and Discussion

3.1 Morphology and structure characterization

Fig.1 shows the XRD patterns of bulk g-C₃N₄, g-C₃N₄ nanoparticles, bare BiFeO₃ and g-C₃N₄/BiFeO₃ samples. For bulk g-C₃N₄, the peaks at 13.0° and 27.4° can be indexed to (100) and (002) crystal planes of the graphite-like carbon nitride, respectively. After the H_2SO_4 treatment, it is seen that the (100) peak of g-C₃N₄ nanoparticles almost disappears which is mainly attributed to the decreased planar size of the g-C₃N₄ layers. Similar phenomenon is also found in the g-C₃N₄ nanosheets prepared though the H_2SO_4 exfoliation of bulk g-C₃N₄[26]. In the XRD pattern of BiFeO₃, all the diffraction peaks are consistent with the standard diffraction data of rhombohedral structured BiFeO₃ (PDF card 74-2016), indicating the preparation of high-quality BiFeO₃. After BiFeO₃ composing with g-C₃N₄, only the characteristic diffraction peaks of BiFeO₃ are observed in the XRD pattern of g-C₃N₄/BiFeO₃ samples, and no traces of g-C₃N₄ are visible. This is possibly due to the low weight loading of g-C₃N₄ and weak diffraction intensity of g-C₃N₄ nanoparticles. Moreover, the impurity peaks cannot be detected in the XRD pattern of composite, suggesting that no any byproducts are generated during the fabrication of the composites.

The chemical functional groups and composition of bulk g-C₃N₄, g-C₃N₄ nanoparticles, bare BiFeO₃ and g-C₃N₄/BiFeO₃ composites were further investigated by FTIR spectrum, as shown in Fig. 2. Most of absorption peaks in the bulk g-C₃N₄ and g-C₃N₄ nanoparticles are the same, indicating that the two g-C₃N₄ samples have similar chemical structure. The sharp absorption peak at about 808 cm⁻¹ belongs to the bending vibration of C-N heterocycles. Several adsorption peaks at 1200-1700 cm⁻¹ are assigned to the stretching vibration of C-N. The typical adsorption peak for the C=N stretching vibration is detected at ~1644 cm⁻¹. As to the spectrum of bare BiFeO₃, the obvious absorption peaks located at around 440 and 560 cm⁻¹ are attributed to the Fe-O stretching and bending vibrations, respectively[31]. For the g-C₃N₄/BiFeO₃ composites, all the characteristic adsorption peaks of g-C₃N₄ nanoparticles and BiFeO₃ can be observed. This suggests that the as-prepared composites are composed of g-C₃N₄ nanoparticles and BiFeO₃. Further observation finds that compared with the absorption peak of C=N stretching vibration (1644 cm⁻¹) for g-C₃N₄ nanoparticles, a slight shift to higher wavenumber in g-C₃N₄/BiFeO₃ composites is detected , indicating the interaction between the two materials.

Fig.3 shows the SEM and HRTEM images of bulk g-C₃N₄, g-C₃N₄ nanoparticles, bare BiFeO₃ and 16CN/BFO samples. It can be seen that bulk g-C₃N₄ exhibits an aggregated layered structure about several micrometers in size (Fig. 3(a)). After H_2SO_4 treatment, the bulk g-C₃N₄ becomes irregular nanoparticles with 30-50 nm in particle size (Fig. 3 (b)). As shown in Fig. 3(c) and (d), the bare BiFeO₃ exhibits regular sphere-like shape with diameter about 30-40 micrometers. The magnified SEM image (Fig. 3(e)) taken from a part of BiFeO₃ microsphere (Fig. 3(d)) shows that the single microsphere is composed of numerous particles with a size of several hundred nanometers and possesses a smooth and clean surface. The SEM image of 16CN/BFO sample obviously displays that the BiFeO₃ microsphere undergo no morphology change in the composite (Fig. 3(f)). The detail view of the sample shows that the g-C₃N₄ nanoparticles are uniformly attached on the surface of BiFeO₃ microspheres (Fig. 3(g)). From the HRTEM image of 16CN/BFO sample (Fig. 3(h)), it is seen that the interplanar spacing of ~0.287
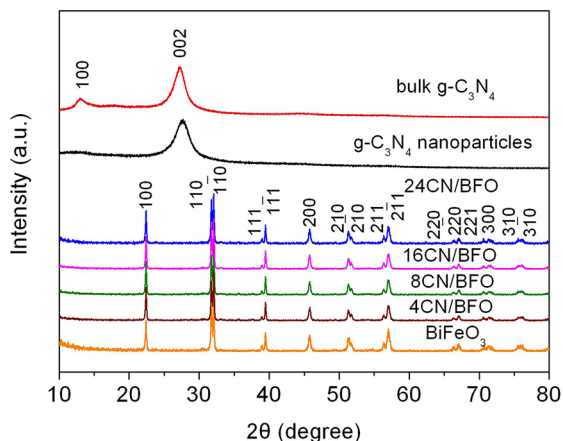
Figure 1. XRD patterns of bulk g-C₃N₄, g-C₃N₄ nanoparticles, BiFeO₃ and g-C₃N₄/BiFeO₃ composites.
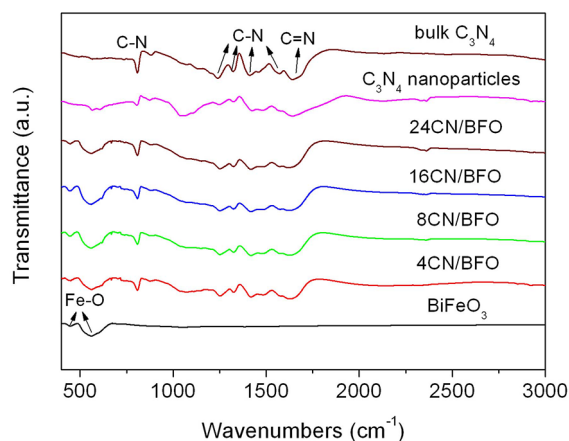
Figure 2. FTIR spectra of bulk g-C₃N₄, g-C₃N₄ nanoparticles, BiFeO₃ and g-C₃N₄/BiFeO₃ composites.
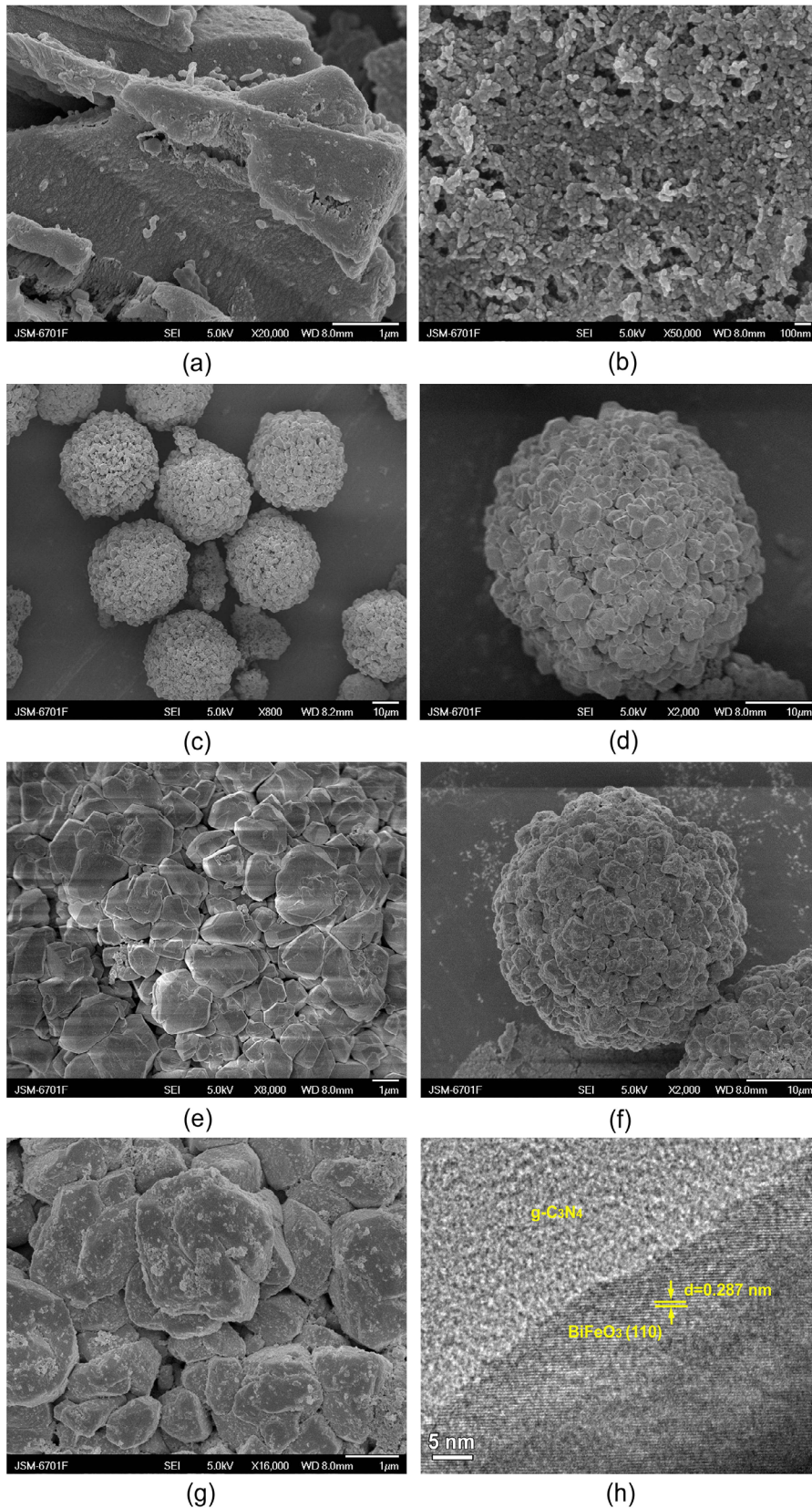
Figure 3. SEM images of bulk g-C$_3$N$_4$ (a), g-C$_3$N$_4$ nanoparticles (b), bare BiFeO$_3$ (c, d and e) and 16CN/ BFO sample (f and g); (h) HRTEM image of 16CN/BFO sample.

nm corresponds to the BiFeO₃ (110) planes and the g-C₃N₄ with low crystallinity is on the edge of BiFeO₃, indicating that the intimate contact between the two materials is formed.

3.2 Optical absorption properties

To study the optical absorption properties of samples, the UV-visible diffuse reflectance spectra of samples are recorded (Fig.4 (a)). Moreover, the corresponding first derivative spectra of the reflectance (R) with respect to wavelength (λ) are also obtained (Fig.4 (b)), in which the peak wavelength are characterized to be the absorption edge of sample. The bandgap energy (E_g) of sample is evaluated by the formula: $E_g = 1240/\lambda_g$, where λ_g is the absorption edge of sample. For the bare g-C₃N₄ samples, one can see from the Fig.4 (b) that the light absorption edge of sample presents a blue shift from ~ 455 nm for the bulk to ~ 430 nm for the nanoparticles. According to these absorption edges, the bandgap energies of bulk g-C₃N₄ and g-C₃N₄ nanoparticles are calculated to be ~ 2.72 and ~ 2.88 eV, respectively. Compared with bulk g-C₃N₄, the enlarged bandgap of g-C₃N₄ nanoparticles is mainly attributed to the quantum confinement effect[32]. As seen from the Fig.4 (b), the absorption edge of BiFeO₃ is located at ~ 563 nm, and the corresponding bandgap energy is estimated to be ~ 2.2 eV. It is worth noting that the g-C₃N₄/BiFeO₃ composites exhibit almost the same absorption edge as BiFeO₃ and g-C₃N₄ nanoparticles, suggesting that BiFeO₃ and g-C₃N₄ nanoparticles undergo no obvious bandgap change in the composites. On the other hand, according to the bandgap energies of BiFeO₃ and g-C₃N₄ nanoparticles, the valence band (VB) and conduction band (CB) potentials of the two materials can be estimated using the following relation (Eq (1) and (2))[33]:

$$E_{VB} = X - E^e + 0.5E_g \qquad (1)$$

$$E_{CB} = X - E^e - 0.5E_g \qquad (2)$$

In the above equation, the X and E^e are the absolute electronegativity of materials (defined as the arithmetic mean of the electron affinity and the first ionization of the constituent atoms) and energy of free electrons on the hydrogen scale (~ 4.5 eV), respectively. The X value of BiFeO₃ is calculated to be 5.93 eV based on the data reported in literatures[34,35], and the X value for g-C₃N₄ nanoparticles is reported to be 4.72 eV[36]. The VB potentials of BiFeO₃ and g-C₃N₄ nanoparticles are calculated to be 2.53 and 1.66 V vs. NHE, and the CB potentials of BiFeO₃ and g-C₃N₄ nanoparticles are estimated to be 0.33 and -1.22 V vs. NHE, respectively.

3.3 Photocatalytic properties

Fig.5 (a) presents the photocatalytic performance for the degradation of MB over g-C₃N₄ nanoparticles, bare BiFeO₃ and g-C₃N₄/BiFeO₃ composites under simulated sunlight irradiation. To clarify the effect of adsorption and direct photolysis of dye on the photocatalytic result, the photolysis and adsorption experimental were performed. It can be seen from Fig.5 (a) that only ~ 17 % of MB is degraded after 9 h simulated sunlight irradiation without catalyst, and the dye is slightly absorbed on the photocatalyst. When BiFeO₃ microspheres are employed as photocatalyst, about 35 % of MB is degraded with 9 h irradiation, indicating its weak photocatalystic activity. After combination with g-C₃N₄ nanoparticles, the g-C₃N₄/BiFeO₃ composites exhibit enhanced phtotcatalytic activity compared with bare BiFeO₃ under the same conditions. In the case of composites, the photocatalytic efficiency gradually increases with the increase of the content of g-C₃N₄ nanoparticles, achieving the highest degradation precentage of ~ 60 % at the g-C₃N₄ nanoparticles content of 16 %. However, further increasing the content of g-C₃N₄ nanoparticles leads to the decrease of
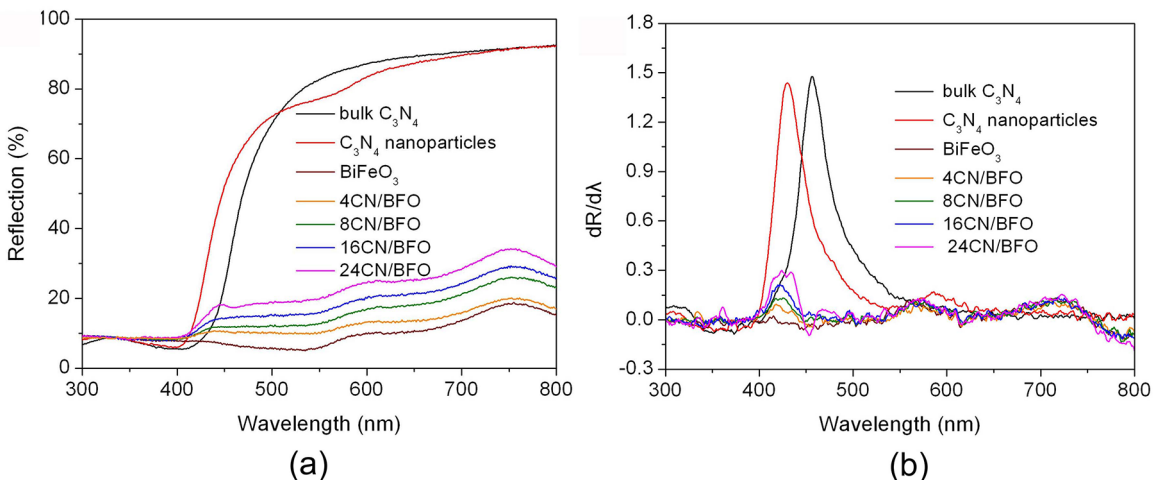
Figure 4. (a) UV-visible diffuse reflectance spectra of bulk g-C₃N₄, g-C₃N₄ nanoparticles, BiFeO₃ and g-C₃N₄/BiFeO₃ composites. (b) the corresponding first derivative of the diffuse reflectance spectra.

photocatalytic efficiency. This is mainly attributed to the fact that the excessive g-C₃N₄ nanoparticles may cover the surface of BiFeO₃ and decrease the photon absorption by the BiFeO₃ microspheres, and moreover, the large amount of g-C₃N₄ nanoparticles tend to self-agglomerate, consequently making it difficult to form heterojunction in the composites. As a consequence, there exists an appropriate ratio of g-C₃N₄ nanoparticles to achieve optimal photocatalytic activity. The experimental data in Fig 5 (a) were fitted by first-order kinetic equation $\ln(C_0/C_t) = k_{app}t$, where k_{app} is the apparent first-order reaction rate constant (Fig 5 (b)). The reaction rate constant of samples are shown in Fig 5 (b) . It can be seen that the 16CN/BFO sample exhibits the highest reaction constant, which is almost 2.1 times as that of bare BiFeO₃.

For comparison, the photocatalytic performances of the physical mixture sample M16CN/BFO and the bulk g-C₃N₄/BiFeO₃ composite (16bulkCN/BFO) toward the degradation of MB were also investigated, as shown in Fig.5 (c). It is seen that the photocatalytic activities of the two samples are much lower than that of 16CN/BFO sample. Compared with physical mixture, the hydrothermal treatment in this work is

more likely to promote the formation of the heterojunction between g-C₃N₄ and BiFeO₃. This is beneficial to the migration of the photogenerated charge between the two materials. On the other hand, it is generally accepted that the g-C₃N₄ nanoparticles exhibit much higher surface area than bulk g-C₃N₄, thus offering more available surface active sites for the photocatalytic reaction. The above results illustrate that the nanoscaled g-C₃N₄ in the composite and strong heterojunction between g-C₃N₄ and BiFeO₃ are necessary for the efficient improvement of photocatalytic activity.

To exclude the dye sensitization effect during the photocatalytic process, phenol is used as another colorless target pollutant to test the photocatalytic activity of BiFeO₃ microspheres and 16CN/BFO sample under simulated sunlight irradiation, as shown in Fig.6 (a). The blank experiment indicates that the direct photolysis of phenol is about 5 % for 9 h without photocatalyst. Bare BiFeO₃ can only degrade ~ 13 % of phenol after 9 h irradiation. The 16CN/BFO sample exhibits improved photocatalytic activity for the degradation of phenol compared with bare BiFeO₃ and about 25 % of phenol is degraded after 9 h
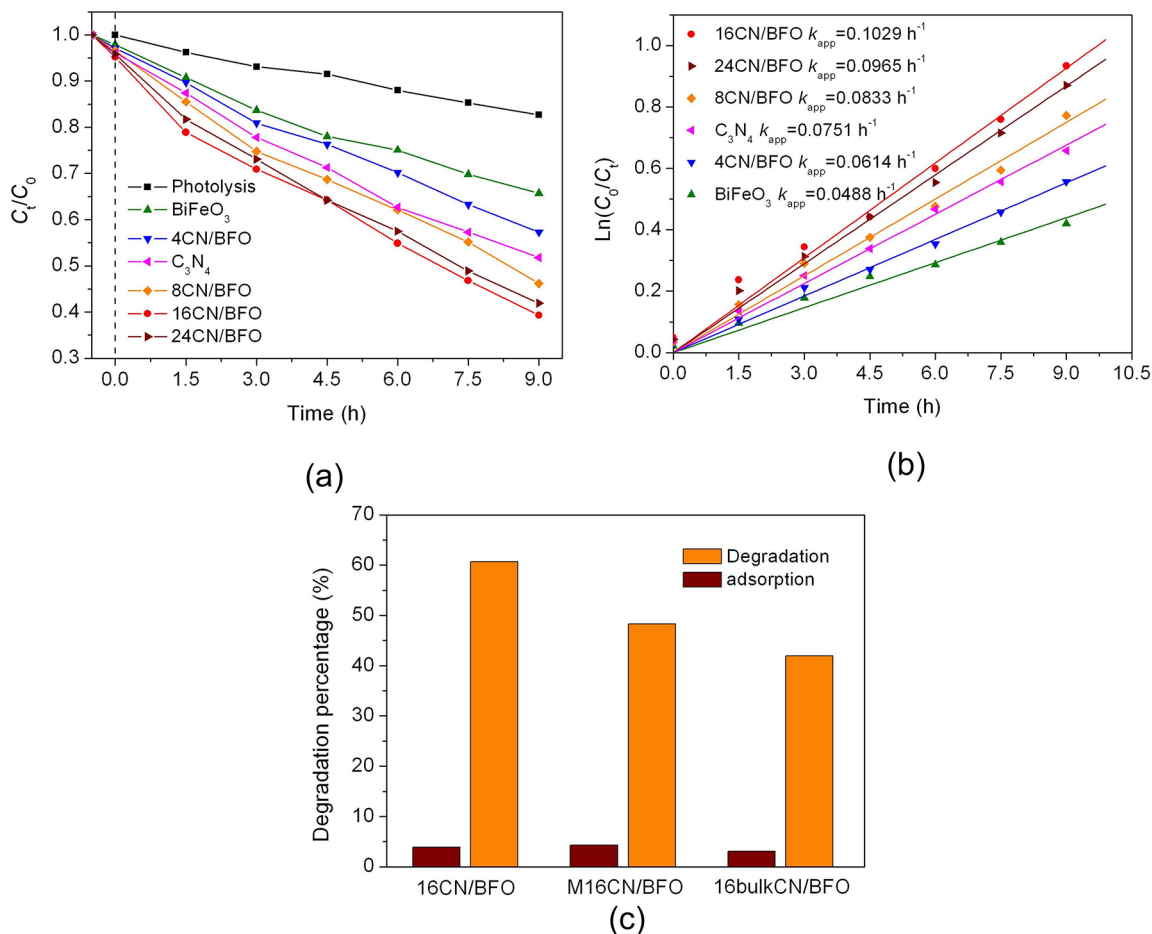
Figure 5. (a) Photocatalytic degradation of MB as a function of irradiation time without catalyst and in the presence of g-C₃N₄ nanoparticles, BiFeO₃ and g-C₃N₄/BiFeO₃ samples. (b) Kinetic plots of the photocatalytic degradation of MB over g-C₃N₄ nanoparticles, BiFeO₃ and g-C₃N₄/BiFeO₃ samples. (c) Degadation percentage and adsorption percentage of MB using 16CN/BFO, M16CN/BFO and 16bulkCN/BFO as photocatalyst at an irradiation time of 9 h. Initial conditions: C(MB) = 5 mg/L, C(catalysts) = 5 mg/L, T = ~ 20ºC.
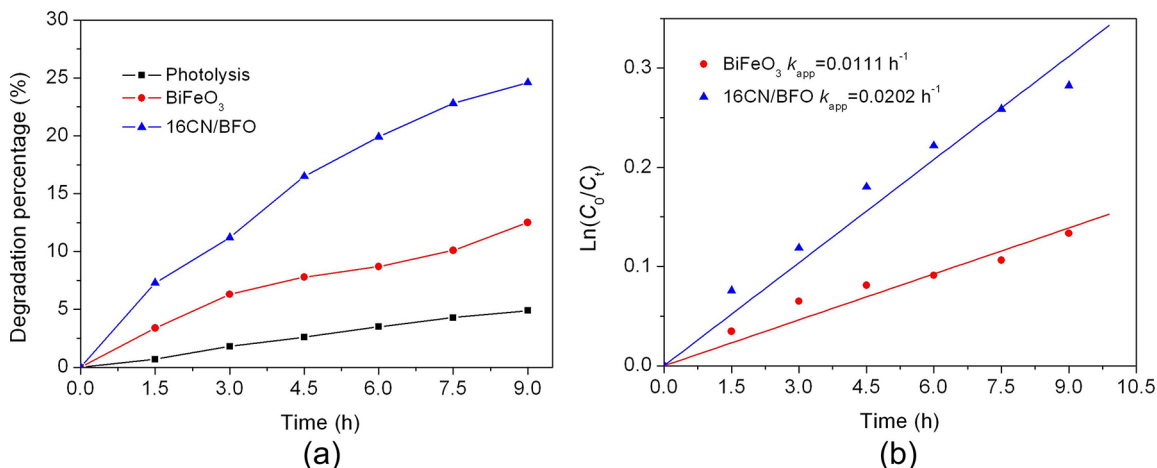
Figure 6. (a) Photocatalytic degradation of phenol versus irradiation time over BiFeO$_3$ and 16CN/BFO sample, along with blank experiment. (b) Kinetic plots of the photocatalytic degradation of phenol over BiFeO$_3$ and 16CN/BFO sample. Initial conditions: C(phenol) = 5 mg/L, C(catalysts) = 0.5 g/L, T = ~ 20ºC.

exposure. The photocatalytic degradation kinetics of phenol is also investigated (Fig.6 (b)), indicating that the reaction rate constant of 16CN/BFO (0.0202 h^{-1}) is higher than that of bare BiFeO$_3$ (0.0111 h^{-1}). The result demonstrated that the degradation of dye over g-C$_3$N$_4$/BiFeO$_3$ composites is caused by its intrinsical photocatalytic property rather than dye sensitization.

In addition to the catalytic activity, the recyclability of photocatalysts is another important parameter for their photocatalytic application. The recycling runs for the photocatalytic degradation of MB over 16CN/BFO sample under simulated sunlight illumination were carried out, as presented in Fig.7. It can be seen that the degradation percentage of dye still reaches ~ 53 % after five successive runs. This indicates that g-C$_3$N$_4$/BiFeO$_3$ composites exhibit good photocatalytic stability for the dye degradation.
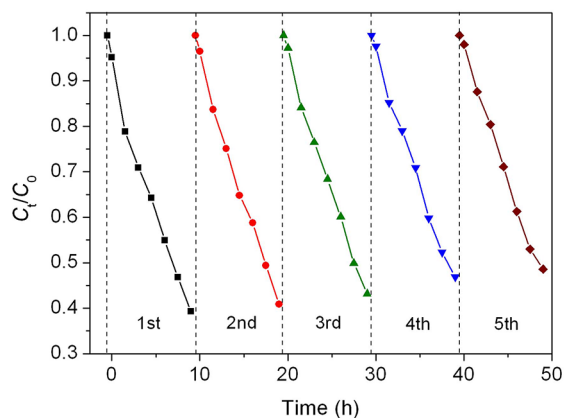
Figure 7. Photocatalytic recyclability of 16CN/BFO sample for the degradation of MB under simulated sunlight irradiation. Initial conditions: C(MB) = 5 mg/L, T = ~ 20ºC.

3.4 Photocatalytic mechanism

In order to clarify the photocatalytic degradation mechanism, the active species trapping experiments were carried out. As shown in Fig. 8, the degradation percentage of MB decreases obviously by the addition of AO (a scavenger of h$^+$), indicating that the photogenerated h$^+$ plays an important role in this photocatalytic reaction. Nevertheless, the photocatalytic degradation of dye is slightly inhibited with the introduction of ethanol (a scavenger of •OH), implying relatively minor role of •OH responsible for the dye degradation. Besides h$^+$ and •OH, •O$_2$ and H$_2$O$_2$ generated from the reaction between photogenerated electrons and O$_2$ are considered to be another active species for dye degradation. It is generally accepted that the O$_2$ molecules dissolved in reaction solution can be expelled by the N$_2$ purging, and then inhibits the generation of •O$_2$ and H$_2$O$_2$. Upon bubbling with N$_2$, a drastic decrease of the degradation percentage is observed, suggesting that •O$_2$ and/or H$_2$O$_2$ is the major active species in the photocatalysis.

Based on the above experimental results, a possible photocatalytic mechanism of g-C$_3$N$_4$/BiFeO$_3$ composite for the degradation of MB is proposed, as displayed in Fig. 9. When the composite is irradiated by simulated sunlight, the g-C$_3$N$_4$ nanoparticles and BiFeO$_3$ are excited and generated photoinduced electron-hole pairs (Eq (3) and (4)). As mentioned above, the CB (-1.22 V) and VB (1.66 V) potentials of g-C$_3$N$_4$ are negative to the CB (0.33 V) and VB (2.53 V) potentials of BiFeO$_3$, respectively, suggesting that the two photocatalysts exhibit matchable overlapping band-structures. Therefore, the photoinduced electrons in the CB of g-C$_3$N$_4$ can facilely migrate to the CB of BiFeO$_3$, meanwhile the photogeneated holes are prone to transfer from the VB of BiFeO$_3$ to that of g-C$_3$N$_4$. Due to the above charge transfer process, the recombination of the photogenerated electrons-holes pairs is inhibited to a large extent, leaving more photogenerated charges to form active
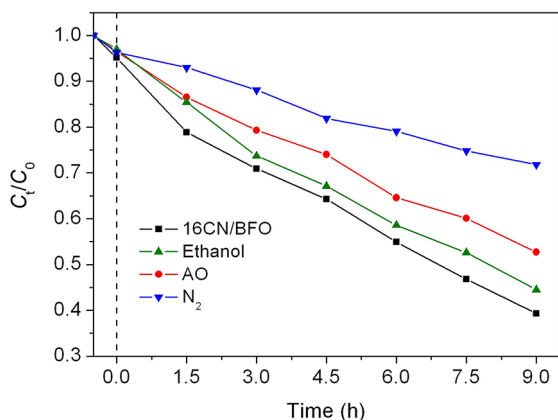
Figure 8. Effect of N_2, ammonium oxalate (AO) and ethanol on the photocatalytic degradation of MB over 16CN/BFO sample. Initial conditions: C(MB) = 5 mg/L, C(catalysts) = 0.5 g/L, C(AO) =2×10^{-3} mol/L, C(ethanol) =10 % by volume, N_2 flow rate = 0.1 L/min, $T = \sim 20ºC$.
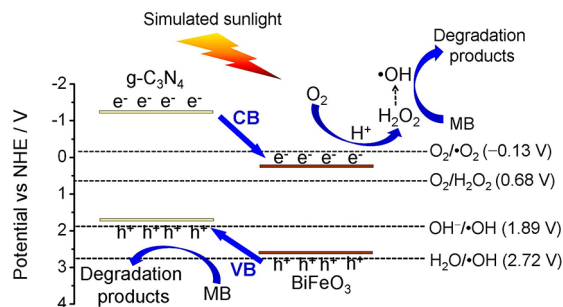
Figure 9. A proposed photocatalytic mechanism of g-C_3N_4/BiFeO$_3$ composite for the degradation of MB under simulated sunlight irradiation.

species, which is beneficial to improving the photocatalytic activity. It is well known that the photogenerated holes in the VB of g-C_3N_4 possess strong ability to oxidize dyes directly. However, because the VB potential of g-C_3N_4 is negative to the redox potentials of H_2O/•OH (+2.72 V vs. NHE) and OH$^-$/•OH (+1.89 V vs. NHE) [37], photogenerated holes cannot oxidize OH$^-$ or H_2O to form •OH radicals. On the other hand, the CB potential of BiFeO$_3$ is more positive than the redox potentials of O_2/•O_2 (-0.13 V vs. NHE) but more negative than that of O_2/H_2O_2 (0.68 V vs. NHE) [38], indicating that the photogenerated electrons in the CB of BiFeO$_3$ cannot reduce O_2 to generate •O_2 but can react with O_2 and H$^+$ to produce H_2O_2 (Eq (5)). The analysis result confirms the role of H_2O_2 for the dye degradation. This is why N_2 purging exhibit obvious inhibiting effect on the photocatalytic efficiency (Fig.8). Furthermore, the H_2O_2 can also take part in a series of reactions to generate •OH radicals (Eq (6)), which is regarded to be the major route for the production of •OH radicals in this photocatalytic process. As a consequence, the photocatalytic degradation of MB over simulated sunlight irradiated g-C_3N_4/BiFeO$_3$ composite is mainly caused by the attack of h$^+$, •OH and

H_2O_2 (Eq (7)). This is consistent with the results of active species trapping experiment.

$$BiFeO_3 + hv \rightarrow BiFeO_3\,(\mathrm{e}^- + \mathrm{h}^+) \qquad (3)$$

$$C_3N_4 + hv \rightarrow C_3N_4\,(\mathrm{e}^- + \mathrm{h}^+) \qquad (4)$$

$$O_2 + 2H^+ + 2e^- \rightarrow H_2O_2 \qquad (5)$$

$$H_2O_2 + hv \rightarrow 2 \cdot OH \qquad (6)$$

$$h^+, H_2O_2 \text{ or } \cdot OH + \mathrm{dye} \rightarrow \mathrm{deg\,radation\ products} \qquad (7)$$
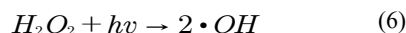
4. Conclusion

The g-C_3N_4 nanoparticles were decorated on the BiFeO$_3$ microspheres through hydrothermal method to obtain g-C_3N_4 nanoparticles/BiFeO$_3$ composites. The as-prepared g-C_3N_4/BiFeO$_3$ composites exhibit much higher photocatalytic activity towards the degradation of MB under simulated sunlight irradiation than bare BiFeO$_3$. Furthermore, the intrinsical photocatalytic property of composite is demonstrated by the degradation of colorless phenol under the same condition. In addition, the composite possess good photocatalytic stability. The enhancement of the photocatalytic activity for the g-C_3N_4/BiFeO$_3$ composite is mainly ascribe to the photoinduced electron-hole pairs separation derived from the charge migration between g-C_3N_4 and BiFeO$_3$. The investigation of phtotcatalytic mechanism of g-C_3N_4/BiFeO$_3$ composite suggests that the main active species responsible for dye degradation are the h$^+$ and H_2O_2, while •OH plays a minor role in the photocatalytic reaction.

5. Acknowledgments

6. References

1. Fujishima A, Zhang X, Tryk DA. Heterogeneous photocatalysis: From water photolysis to applications in environmental cleanup. *International Journal of Hydrogen Energy*. 2007;32(14):2664-2672.

2. Zheng CX, Yang H, Cui ZM, Zhang HM, Wang XX. A novel Bi$_4$Ti$_3$O$_{12}$/Ag$_3$PO$_4$ heterojunction photocatalyst with enhanced photocatalytic performance. *Nanoscale Research Letters*. 2017;12:608.

3. Zhao J, Yang Y, Dong XT, Ma QL, Yu WS, Wang JX, et al. Electrospinning construction of Bi$_2$WO$_6$/RGO composite nanofibers with significantly enhanced photocatalytic water splitting activity. *RSC Advances*. 2016;6(69):64741-64748.

4. Xu S, Wang XL, Dong XT, Yu WS, Wang JX, Liu GX. Novel construction technique, structure and photocatalysis of Y$_2$O$_2$CN$_2$ nanofibers and nanobelts. *RSC Advances*. 2016;6(49):43322-43329.

5. Cheng L, Li D, Dong XT, Ma QL, Yu WS, Wang JX, et al. A new route to fabricate PbS nanofibers and PbSe nanofibers via electrospinning combined with double-crucible technique. J*ournal of Materials Science: Materials in Electronics*. 2016;27(9):9772-9779.

6. Zhao J, Yang Y, Yu WS, Ma QL, Dong XT, Wang XL, et al. Bi$_2$MoO$_6$/RGO composite nanofibers: facile electrospinning fabrication, structure, and significantly improved photocatalytic water splitting activity. Journal of Materials Science: *Materials in Electronics*. 2017;28(1):543-552.

7. Morín MEZ, Torres-Martínez L, Sanchez-Martínez D, Gómez-Solís C. Photocatalytic Performance of Titanates with Formula MTiO$_3$ (M= Fe, Ni, and Co) Synthesized by Solvo-Combustion Method. *Materials Research*. 2017;20(5):1322-1331.

8. Di LJ, Yang H, Xian T, Chen XJ. Enhanced Photocatalytic Activity of NaBH$_4$ Reduced BiFeO$_3$ Nanoparticles for Rhodamine B Decolorization. *Materials (Basel)*. 2017;10(10):1118.

9. Wei J, Zhang C, Xu Z. Low-temperature hydrothermal synthesis of BiFeO$_3$ microcrystals and their visible-light photocatalytic activity. *Materials Research Bulletin*. 2012;47(11):3513-3517.

10. Gao F, Chen XY, Yin KB, Dong SA, Ren ZF, Yuan F, et al. Visible-Light Photocatalytic Properties of Weak Magnetic BiFeO$_3$ Nanoparticles. *Advanced Materials*. 2007;19(19):2889-2892.

11. Ji W, Yao K, Lim YF, Liang YC, Suwardi A. Epitaxial ferroelectric BiFeO$_3$ thin films for unassisted photocatalytic water splitting. *Applied Physics Letters*. 2013;103(6):062901.

12. Chen YC, He Q, Chu FN, Huang YC, Chen JW, Liang WI, et al. Electrical Control of Multiferroic Orderings in Mixed-Phase BiFeO$_3$ Films. *Advanced Materials*. 2012;24(22):3070-3075.

13. Chen CC, Fan T. Study on carbon quantum dots/BiFeO$_3$ heterostructures and their enhanced photocatalytic activities under visible light irradiation. *Journal of Materials Science: Materials in Electronics*. 2017;28(14):10019-10027.

14. Vanga PR, Mangalaraja RV, Ashok M. Effect of co-doping on the optical, magnetic and photocatalytic properties of the Gd modified BiFeO$_3$. *Journal of Materials Science: Materials in Electronics*. 2016;27(6):5699-5706.

15. Tovstolytkin NA, Lotey GS. Plasmonic Enhanced Photocatalytic Activity of Ag Nanospheres Decorated BiFeO$_3$ Nanoparticles. *Catalysis Letters*. 2017;147(7):1640-1645.

16. Fan T, Chen CC, Tang ZG. Hydrothermal synthesis of novel BiFeO$_3$/BiVO$_4$ heterojunctions with enhanced photocatalytic activities under visible light irradiation. *RSC Advances*. 2016;6(12):9994-10000.

17. Wang L, Niu CG, Wang Y, Wang Y, Zeng GM. The synthesis of Ag/AgCl/BiFeO$_3$ photocatalyst with enhanced visible photocatalytic activity. *Ceramics International*. 2016;42(16):18605-18611.

18. Guo R, Fang L, Dong W, Zheng F, Shen M. Magnetically separable BiFeO$_3$ nanoparticles with a γ-Fe$_2$O$_3$ parasitic phase: controlled fabrication and enhanced visible-light photocatalytic activity. *Journal of Materials Chemistry*. 2011;21(46):18645-18652.

19. Zhang T, Shen Y, Qin YH, Liu Y, Xiong R, Shi J, et al. Facial Synthesis and Photoreaction Mechanism of BiFeO$_3$/Bi$_2$Fe$_4$O$_9$ Heterojunction Nanofibers. *ACS Sustainable Chemistry & Engineering*. 2017;5(6):4630-4636.

20. Fang LJ, Li YH, Liu PF, Wang DP, Zeng HD, Wang XL, et al. Facile Fabrication of Large-Aspect-Ratio g-C$_3$N$_4$ Nanosheets for Enhanced Photocatalytic Hydrogen Evolution. *ACS Sustainable Chemistry & Engineering*. 2017;5(3):2039-2043.

21. Xu J, Zhang L, Shi R, Zhu Y. Chemical exfoliation of graphitic carbon nitride for efficient heterogeneous photocatalysis. *Journal of Materials Chemistry A*. 2013;1(46):14766-14772.

22. Cui ZM, Yang H, Zhao XX. Enhanced photocatalytic performance of g-C$_3$N$_4$/Bi$_4$Ti$_3$O$_{12}$ heterojunction nanocomposites. *Materials Science and Engineering: B*. 2018;229:160-172.

23. Mamba G, Mishra AK. Graphitic carbon nitride (g-C$_3$N$_4$) nanocomposites: A new and exciting generation of visible light driven photocatalysts for environmental pollution remediation. *Applied Catalysis B: Environmental*. 2016;198:347-377.

24. Wang X, Mao W, Zhang J, Han Y, Quan C, Zhang Q, et al. Facile fabrication of highly efficient g-C$_3$N$_4$/BiFeO$_3$ nanocomposites with enhanced visible light photocatalytic activities. *Journal of Colloid and Interface Science*. 2015;448:17-23.

25. Fan T, Chen C, Tang Z, Ni Y, Lu C. Synthesis and characterization of g-C$_3$N$_4$/BiFeO$_3$ composites with an enhanced visible light photocatalytic activity. *Materials Science in Semiconductor Processing*. 2015;40:439-445.

26. Tong J, Zhang L, Li F, Li M, Cao S. An efficient top-down approach for the fabrication of large-aspect-ratio g-C$_3$N$_4$ nanosheets with enhanced photocatalytic activities. *Physical Chemistry Chemical Physics*. 2015;17(36):23532-23537.

27. Ye Y, Yang H, Wang X, Feng W. Photocatalytic, Fenton and photo-Fenton degradation of RhB over Z-scheme g-C$_3$N$_4$/LaFeO$_3$ heterojunction photocatalysts. *Materials Science in Semiconductor Processing*. 2018;82:14-24.

28. Di LJ, Yang H, Xian T, Li RS, Feng YC, Feng WJ. Influence of precursor Bi^{3+}/Fe^{3+} ion concentration on hydrothermal synthesis of BiFeO$_3$ crystallites. *Ceramics International*. 2014;40(3):4575-4578.

29. Daneshvar N, Salari D, Khataee AR. Photocatalytic degradation of azo dye acid red 14 in water: investigation of the effect of operational parameters. *Journal of Photochemistry and Photobiology A: Chemistry*. 2003;157(1):111-116.

30. Wang F, Yang H, Zhang YC. Enhanced photocatalytic performance of CuBi$_2$O$_4$ particles decorated with Ag nanowires. *Materials Science in Semiconductor Processing*. 2018;73:58-66.

31. Xian T, Yang H, Shen X, Jiang JL, Wei ZQ, Feng WJ. Preparation of high-quality BiFeO$_3$ nanopowders via a polyacrylamide gel route. *Journal of Alloys and Compounds*. 2009;480(2):889-892.

32. Li J, Yin Y, Liu E, Ma Y, Wan J, Fan J, et al. In situ growing Bi$_2$MoO$_6$ on g-C$_3$N$_4$ nanosheets with enhanced photocatalytic hydrogen evolution and disinfection of bacteria under visible light irradiation. *Journal of Hazardous Materials*. 2017;321:183-192.

33. Zhao X, Yang H, Cui Z, Li R, Feng W. Enhanced photocatalytic performance of Ag-Bi$_4$Ti$_3$O$_{12}$ nanocomposites prepared by a photocatalytic reduction method. *Materials Technology*. 2017;32(14):870-880.

34. Hotop H, Lineberger WC. Binding energies in atomic negative ions. *Journal of Physical and Chemical Reference Data*. 1975;4(3):539-576.

35. Andersen T, Haugen HK, Hotop H. Binding Energies in Atomic Negative Ions: III. *Journal of Physical and Chemical Reference Data*. 1999;28(6):1511-1533.

36. Meng J, Pei J, He Z, Wu S, Lin Q, Wei X, et al. Facile synthesis of g-C$_3$N$_4$ nanosheets loaded with WO$_3$ nanoparticles with enhanced photocatalytic performance under visible light irradiation. *RSC Advances*. 2017;7(39):24097-24104.

37. Tachikawa T, Fujitsuka M, Majima T. Mechanistic Insight Into the TiO$_2$ Photocatalytic Reactions: Design of New Photocatalysts. *Journal of Physical Chemistry C*. 2007;111(14):5259-5275.

38. Teoh WY, Scott JA, Amal R. Progress in Heterogeneous Photocatalysis: From Classical Radical Chemistry to Engineering Nanomaterials and Solar Reactors. *Journal of Physical Chemistry Letters*. 2012;3(5):629-639.